

Strength increase during ceramic biomaterial-induced bone regeneration: a micromechanical study

Stefan Scheiner  · Vladimir S. Komlev · Christian Hellmich

Received: 29 January 2016 / Accepted: 4 October 2016 / Published online: 20 October 2016
© The Author(s) 2016. This article is published with open access at Springerlink.com

Abstract Bone tissue engineering materials must blend in the targeted physiological environment, in terms of both the materials' biocompatibility and mechanical properties. As for the latter, a well-adjusted stiffness ensures that the biomaterial's deformation behavior fits well to the deformation behavior of the surrounding biological tissue, whereas an appropriate strength provides sufficient load-carrying capacity of the biomaterial. Here, a mathematical modeling approach for estimating the macroscopic load that initiates failure of a hierarchically organized, granular, hydroxyapatite-based biomaterial is presented. For this purpose, a micromechanics model is developed for downscaling macroscopically prescribed stress (or strain) states to the level of the needle-shaped hydroxyapatite crystals. Presuming that the biomaterial fails due to the quasi-brittle failure of the most unfavorably stressed hydroxyapatite needle, the downscaled stress tensors are fed into a suitable, Mohr-Coulomb-

type failure criterion, based on which the macroscopic failure load is deduced. The change of the biomaterial's composition in response to placing it in physiological solution, caused by growth of new bone tissue on the granules's surfaces, on the one hand, and by resorption of the hydroxyapatite crystals, on the other hand, is taken into account by means of suitable evolution laws. Numerical studies show how the macroscopic load-carrying capacity of the biomaterial is influenced by its design parameters. The presented modeling approach could prove beneficial for the design process of the studied biomaterials (as well as similarly composed biomaterials), particularly in terms of optimizing its mechanical performance.

Keywords Continuum micromechanics · Elastic limit · Multiscale modeling · Bone ingrowth · Tissue engineering

S. Scheiner (✉) · C. Hellmich
Institute for Mechanics of Materials and Structures,
Vienna University of Technology, Vienna, Austria
e-mail: stefan.scheiner@tuwien.ac.at

V. S. Komlev
A.A. Baikov Institute of Metallurgy and Materials Science,
Russian Academy of Sciences, Moscow, Russia

V. S. Komlev
Institute of Laser and Information Technologies, Russian
Academy of Sciences, Moscow, Russia

Abbreviations

gran	Granule material (RVE II)
μ CT	Micro-computed tomography
polyHA	Hydroxyapatite polycrystal (RVE I)
RVE	Representative volume element
congl	Conglomerate of granules coated with bone tissue (RVE III)

Latin symbols

A_{HA}^{polyHA}	Fourth-order strain concentration tensor of hydroxyapatite crystal needles in hydroxyapatite polycrystal
A_{polyHA}^{gran}	Fourth-order strain concentration tensor of hydroxyapatite polycrystal in granule material
B_{HA}^{polyHA}	Fourth-order stress concentration tensor of hydroxyapatite crystal needles in hydroxyapatite polycrystal
B_{polyHA}^{gran}	Fourth-order stress concentration tensor of hydroxyapatite polycrystal in granule material
C_{bone}	Fourth-order stiffness tensor of bone tissue
C_{gran}	Fourth-order stiffness tensor of granular material
C_{H_2O}	Fourth-order stiffness tensor of water
C_{HA}	Fourth-order stiffness tensor of hydroxyapatite crystals
$C_{macro\phi}$	Fourth-order stiffness tensor of macropores
$C_{meso\phi}$	Fourth-order stiffness tensor of mesopores
$C_{micro\phi}$	Fourth-order stiffness tensor of micropores
C_{polyHA}	Fourth-order stiffness tensor of hydroxyapatite polycrystal
C_{congl}	Fourth-order stiffness tensor of bone-scaffold conglomerate
D_k	Material parameter
d	Characteristic length of an inhomogeneity within a representative volume element
e	Crack density parameter
e_1, e_2, e_3	Unit base vectors of a Cartesian base system
$e_r, e_\vartheta, e_\varphi$	Unit base vectors of a spherical coordinate system
E_{HA}	Young's modulus of hydroxyapatite crystals
E_{congl}	Second-order strain tensor of the bone-scaffold conglomerate
$E_{congl,ij}$	Components of E_{congl} ($i, j = 1, 2, 3$)
f_{bone}^{congl}	Volume fraction of bone tissue within bone-scaffold conglomerate

f_{gran}^{congl}	Volume fraction of the granules within bone-scaffold conglomerate
f_{HA}^{polyHA}	Volume fraction of the hydroxyapatite needles within hydroxyapatite polycrystal
f_{polyHA}^{gran}	Volume fraction of the microporous hydroxyapatite matrix within granule material
$f(\sigma)$	Failure function formulated in terms of stress tensor σ
I	Second-order unit tensor
II	Fourth-order unit tensor
J	Deviatoric part of the fourth-order unit tensor
k_{gran}	Bulk modulus of the granule material
k_{growth}	Formation rate of bone tissue
k_{H_2O}	Bulk modulus of water
k_{HA}	Bulk modulus of the hydroxyapatite crystals
k_{res}	Resorption rate of hydroxyapatite crystals
k_{congl}	Bulk modulus of the bone-scaffold conglomerate
K	Volumetric part of the fourth-order unit tensor
ℓ	Characteristic length of a representative volume element
\mathcal{L}	Characteristic length of a structure made up the material defined on the level of a representative volume element
n	Vector oriented perpendicular to unit base vector e_r
P_{cyl}^{polyHA}	Fourth-order Hill tensor of cylindrical inclusions in a matrix with stiffness C_{polyHA}
P_{sph}^{polyHA}	Fourth-order Hill tensor of spherical inclusions in a matrix with stiffness C_{polyHA}
Q	Second-order transformation tensor
Q	Fourth-order tensor defined through Poisson's ratio ν_{polyHA}
r_{gran}	Granule radius
t	Time variable

Greek symbols

$\Gamma_{gran,1}^k$	Material parameter
---------------------	--------------------

$\Gamma_{\text{gran},1}^{\mu}$	Material parameter	Σ_{congl}	Second-order stress tensor of bone-scaffold conglomerate
$\Gamma_{\text{gran},2}^{\mu}$	Material parameter	$\Sigma_{\text{congl},ij}$	Component of Σ_{congl} ($i, j = 1, 2, 3$)
$\epsilon_{\text{polyHA}}^{\text{polyHA}}$	Second-order strain tensor of hydroxyapatite crystals in hydroxyapatite polycrystal	$\Sigma_{\text{congl},11}^{\text{ult}}$	Component in direction \mathbf{e}_1 of the second-order stress tensor of bone-scaffold conglomerate representing the ultimate loading
$\epsilon_{\text{gran}}^{\text{congl}}$	Second-order strain tensor of granule material in bone-scaffold conglomerate	$\phi_{\text{macro}}^{\text{congl}}$	Volume fraction of macropores in bone-scaffold conglomerate
$\epsilon_{\text{gran}}^{\text{congl,dev}}$	Second-order deviatoric strain tensor of granule material in bone-scaffold conglomerate	$\phi_{\text{meso}}^{\text{gran}}$	Volume fraction of mesopores in granule material
$\epsilon_{\text{gran}}^{\text{congl,vol}}$	Second-order volumetric strain tensor of granule material in bone-scaffold conglomerate	$\phi_{\text{micro}}^{\text{polyHA}}$	Volume fraction of micropores in hydroxyapatite polycrystal
$\epsilon_{\text{polyHA}}^{\text{gran}}$	Second-order strain tensor of hydroxyapatite polycrystal in granule material	φ	Angle defining the orientation of the spherical coordinate system ($\mathbf{e}_r, \mathbf{e}_\vartheta, \mathbf{e}_\varphi$)
ϑ	Angle defining the orientation of the spherical coordinate system ($\mathbf{e}_r, \mathbf{e}_\vartheta, \mathbf{e}_\varphi$)	ψ	Angle defining orientation of vector \mathbf{n}
μ_{gran}	Shear modulus of granule material		
μ_{HA}	Shear modulus of hydroxyapatite crystals		
μ_{congl}	Shear modulus of bone-scaffold conglomerate		
ν_{gran}	Poisson's ratio of granule material		
ν_{HA}	Poisson's ratio of hydroxyapatite crystals		
ν_{polyHA}	Poisson's ratio of hydroxyapatite polycrystal		
$\sigma_{\text{HA}}^{\text{polyHA}}$	Second-order stress tensor of hydroxyapatite crystals in hydroxyapatite polycrystal		
$\sigma_{\text{HA},ij}^{\text{polyHA}}$	Component of $\sigma_{\text{HA}}^{\text{polyHA}}$ ($i, j = 1, 2, 3$)		
$\sigma_{\text{HA}}^{\text{ult,s}}$	Shear strength of hydroxyapatite crystals		
$\sigma_{\text{HA}}^{\text{ult,t}}$	Tensile strength of hydroxyapatite crystals		
$\sigma_{\text{gran}}^{\text{congl}}$	second-order stress tensor of granule material in bone-scaffold conglomerate		
$\sigma_{\text{gran}}^{\text{congl,dev}}$	Second-order deviatoric stress tensor of granule material in bone-scaffold conglomerate		
$\sigma_{\text{gran}}^{\text{congl,vol}}$	Second-order volumetric stress tensor of granule material in bone-scaffold conglomerate		
$\sigma_{\text{gran},ij}^{\text{congl}}$	Component of $\sigma_{\text{gran}}^{\text{congl}}$ ($i, j = 1, 2, 3$)		
$\sigma_{\text{polyHA}}^{\text{gran}}$	Second-order stress tensor of hydroxyapatite polycrystal in granule material		
$\sigma_{\text{polyHA},ij}^{\text{gran}}$	Component of $\sigma_{\text{polyHA}}^{\text{gran}}$ ($i, j = 1, 2, 3$)		

1 Introduction

The field of bone tissue engineering aims at the reinforcing or even replacing diseased (or for other reasons malfunctioning) bone tissue by scaffold structures that are specifically engineered, for blending in the targeted physiological environment, i.e. the immediate vicinity of bone tissue, as well as possible (Burg et al. 2000; Reichert and Hutmacher 2011). From a mechanical point of view, careful tuning of such scaffold structures (and of the materials which they are made of) is called for because contradictory requirements must be brought in line—scaffold structures must be stiff enough to sustain all relevant mechanical load cases, but also soft enough to facilitate, through mechanobiological couplings (Klein-Nulend et al. 2005; Porter et al. 2009; Velasco et al. 2015), the integration into their bony environment. In this regard, two mechanical properties are of particular interest, both on material and structural levels: the stiffness, governing the elastic deformation behavior and therefore the forces attracted by the involved macro- and microstructures; as well as the strength, indicating the stress level that induces material failure.

In the present paper, we study one specific scaffold material that has been developed as bone replacement material with the human mandible as targeted application area (Komlev et al. 2002, 2003). This biomaterial is produced in form of porous, pre-cracked granules, composed of hydroxyapatite as main constituent, but

also including various kinds of pore spaces of distinctively different characteristic lengths. After exposing this biomaterial to the targeted physiological environment prevailing in the immediate vicinity of mandibular bone tissue, two mechanisms are triggered, causing a progressing change of the material's composition over time. On the one hand, bone tissue grows on the granule surfaces, while, on the other hand, concurrently the hydroxyapatite crystals are resorbed—in the long run, the scaffold material merges with the surrounding bone tissue.

In a first approach to analyzing their mechanical behavior, these granules underwent micro-computed tomography (μ CT), and the resulting scans served as basis for combined Finite Element/micromechanics-based simulations (Dejaco et al. 2012, 2016). Here, as a (computationally more efficient) complement, we present a three-step, fully continuum micromechanics-based macro-to-meso-to-micro (stress and strain) downscaling scheme, linking in the end the quasi-brittle failure of single micrometer- or sub-micrometer-sized hydroxyapatite crystal needles to the overall strength of both millimeter-sized biomaterial scaffolds and composites comprising biomaterial scaffold and bone tissue, respectively. For this purpose, a number of homogenization concepts are adapted, extended, and combined, considering the pioneering contributions of Eshelby (1957), Hill (1963, 1965), Laws (1977, 1985), Hervé and Zaoui (1993); and also considering more recent contributions of Deudé et al. (2002), Dormieux et al. (2004), Fritsch et al. (2006), Bertrand and Hellmich (2009). Following Fritsch et al. (2009a, b), we feed the stress of the most unfavorably loaded hydroxyapatite needle into a suitable, Mohr-Coulomb-type failure criterion, and deduce then therefrom the corresponding ultimate macroscopic load bearable by the aforementioned granular, hydroxyapatite-based biomaterial (optionally containing ingrown bone tissue).

After introducing the fundamental modeling concept, together with the chosen model representation of the studied biomaterial, see Sect. 2, a mathematical model for downscaling of the mechanical loading, from the macroscopic to the hydroxyapatite needle scale, is presented, see Sect. 3. Then, a suitable failure criterion is elaborated in Sect. 4.1, and numerical studies show how the macroscopic mechanical loading inducing single hydroxyapatite needle failure changes with varying biomaterial composition. In

order to simulate bone regeneration (which occurs after having placed the biomaterial in the targeted physiological environment), involving bone growth and scaffold resorption, suitable evolution laws are introduced, and the effects of different material input parameters on the model-predicted development of the load-carrying capacity over time are studied, see Sect. 5. A brief discussion closes the paper, see Sect. 6.

2 Material and methods

2.1 Characterization of the multi-porous hydroxyapatite tissue engineering scaffold material

The biomaterial investigated in this paper is a granular scaffold material, with the granules composed of carbonate-containing hydroxyapatite, the chemical composition of which reads as $\text{Ca}_{10}(\text{PO}_4)_6(\text{OH})_{1.9}(\text{CO}_3)_{0.05}$. This material is produced based on the effect of immiscible liquids (Komlev et al. 2002, 2003), giving access to granules with diameters ranging from 50 to 2000 μm , with the technically relevant granule diameter being approximately 1800 μm (Dejaco et al. 2012).

Several morphological features of these granules can be observed, see the column on the left-hand side of Fig. 1. Firstly, the granules contain pores of two different characteristic lengths: small pores, with a characteristic length ranging from less than one to several micrometers (Dejaco et al. 2016)—these pores are termed “micropores” hereafter; and large pores, with a characteristic length of several hundred micrometers—these pores are termed “mesopores” hereafter. A composite of randomly oriented hydroxyapatite crystals and the micropores constitutes the “base material” of the granules. Increasing the observation scale by several orders of magnitude, one can discern, besides the mesopores, cracks pervading the granule body. Finally, the scaffold material is made up of the above described granules, with pore space in-between—due to the characteristic length of these pores, which is approximately equal to the granule diameter, they are termed “macropores” in the remainder of this paper.

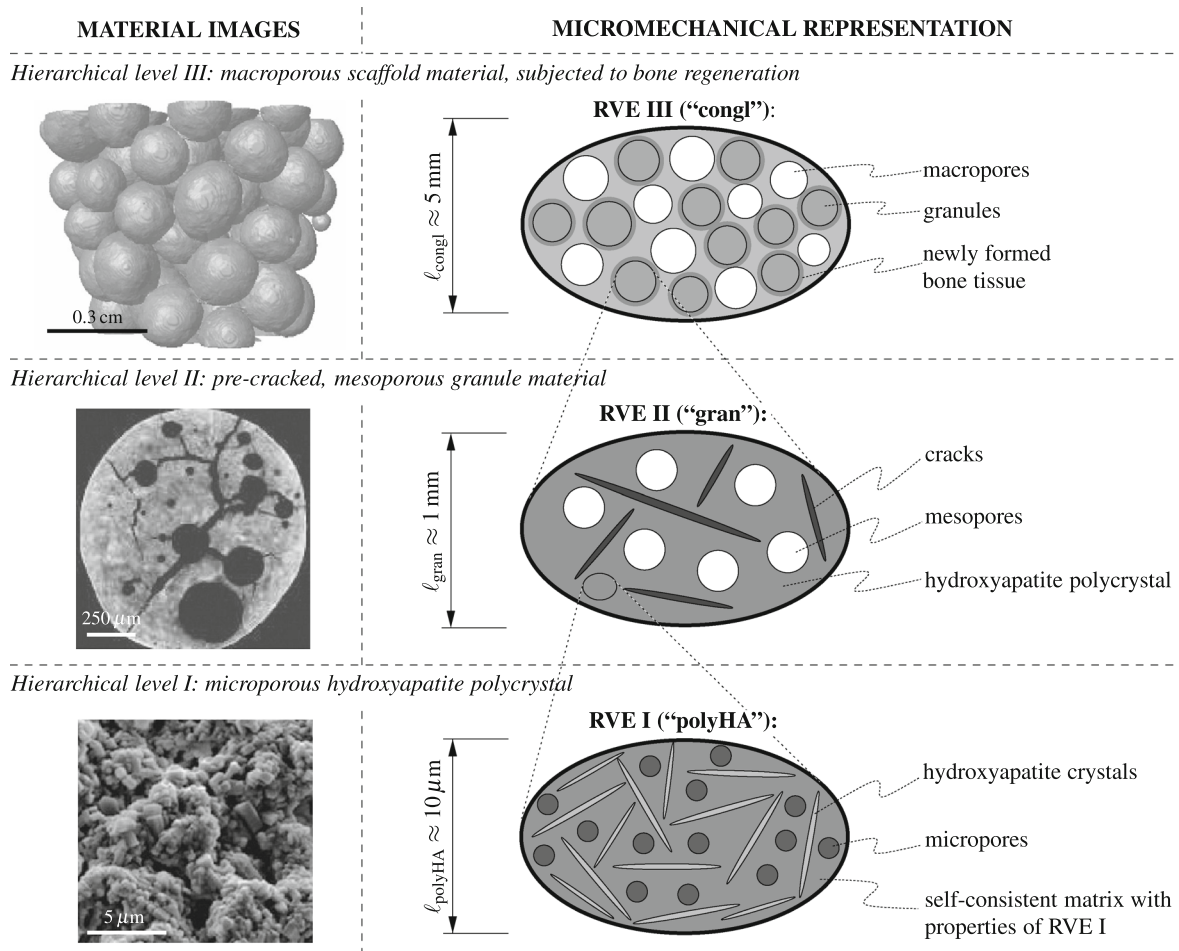


Fig. 1 Three-level micromechanical representation of the hydroxyapatite-based granular biomaterial (*column on the right-hand side*), following the morphological features found in images on different observation scales (*column on the left-hand side*);

the depicted images have been acquired by means of scanning electron microscopy (hierarchical level I) and μ CT imaging techniques (hierarchical levels II and III)

2.2 Fundamentals of continuum micromechanics: the representative volume element

A method particularly well suited for modeling the mechanical behavior of the material described in Sect. 2.1 is continuum micromechanics (Hill 1963; Zaoui 1997, 2002), where a material is understood as a micro-heterogeneous body filling a macro-homogeneous representative volume element (RVE) with characteristic length ℓ , $\ell \gg d$, d standing for the characteristic length of inhomogeneities within the RVE, and $\ell \ll \mathcal{L}$, \mathcal{L} standing for the characteristic lengths of geometry or loading of a structure built up by the mater-

ial defined on the RVE. It should be noted the aforementioned requirements of “much larger” (\gg) and “much smaller” (\ll), respectively, have been shown to be already satisfied if the respective characteristic lengths are separated by a factor of two to three and five to ten, respectively (Drugan and Willis 1996; Kohlhauser and Hellmich 2013).

In general, the microstructure within an RVE is too complicated to be described in complete detail. Therefore, quasi-homogeneous subdomains with known physical properties (such as volume fractions and mechanical properties) are reasonably chosen. They are called material phases. The homogenized (upscaled)

behavior of the material on the observation scale of the RVE, i.e. the relation between homogeneous deformations acting on the boundary of the RVE and resulting macroscopic (average) stresses, can then be estimated from the mechanical behavior of the material phases, their volume fractions within the RVE, their characteristic shapes, and their interactions. If a single material phase is micro-heterogeneous itself, its mechanical behavior can be estimated by introduction of RVEs within this phase, with characteristic lengths $\ell_1 \leq d$, comprising again inhomogeneities with characteristic length $d_1 \ll \ell_1$, and so on. Such an approach is referred to as multi-step homogenization and provides, eventually, access to “universal” phase properties at sufficiently low observation scales (Fritsch and Hellmich 2007).

2.3 Micromechanical modeling

Having in mind the concept of “separation of scales”, as introduced in Sect. 2.2, the following three-level micromechanical representation emerges for the biomaterial under investigation:

On *hierarchical level I*, a microporous, overall isotropic, hydroxyapatite polycrystal is composed of spherical micropores (with volume fraction $\phi_{\text{micro}}^{\text{polyHA}}$), which interact mutually with randomly oriented cylindrical hydroxyapatite crystals (with volume fraction $f_{\text{HA}}^{\text{polyHA}} = 1 - \phi_{\text{micro}}^{\text{polyHA}}$). Typically, the microporosity amounts to $\phi_{\text{micro}}^{\text{polyHA}} = 0.445$ (Dejaco et al. 2012). The characteristic length of the polycrystalline RVE I is in the order of 10 μm , see the bottom row of Fig. 1, with a scanning electron micrograph of the granule nanostructure on the left-hand side and the corresponding RVE I on the right-hand side. In terms of stiffness upscaling, the mutual mechanical interaction of all phases within RVE I calls for a self-consistent homogenization scheme, as introduced by (Fritsch et al. 2006), giving access to the stiffness tensor of the microporous hydroxyapatite polycrystal, $\mathbb{C}_{\text{polyHA}}$, based on the composition and morphology of RVE I, as well as on the stiffness tensors of the hydroxyapatite crystals, \mathbb{C}_{HA} , and of the micropores, $\mathbb{C}_{\text{micro}\phi}$.

On *hierarchical level II*, penny-shaped cracks (with vanishing volume fraction) and spherical mesopores (with volume fraction $\phi_{\text{meso}}^{\text{gran}}$) are embedded in the polycrystal matrix with properties arising from the structure of RVE I, this matrix filling within RVE II the

volume fraction $f_{\text{polyHA}}^{\text{gran}} = 1 - \phi_{\text{meso}}^{\text{gran}}$. Typically, the mesoporosity comes to $\phi_{\text{meso}}^{\text{gran}} = 0.189$ (Dejaco et al. 2012). The characteristic length of RVE II is in the order of 1 mm, see the middle row in Fig. 1, with a micro-computed tomography (μCT) image of the microstructure within a granule on the left-hand side and the corresponding RVE II on the right-hand side. The distinctive matrix-inclusion morphology of RVE II—i.e. cracks and mesopores can be considered as inclusions embedded in the hydroxyapatite polycrystal matrix—suggests the use of a Mori-Tanaka-type homogenization scheme (Mori and Tanaka 1973; Benveniste 1987) for stiffness homogenization; mathematical treatment of the penny-shaped cracks has been dealt with by Deudé et al. (2002), Dormieux et al. (2004). The stiffness tensor of the pre-cracked, mesoporous granule material, \mathbb{C}_{gran} is then governed by the composition and morphology of RVE II, as well as by the stiffness tensors of the hydroxyapatite polycrystal matrix, $\mathbb{C}_{\text{polyHA}}$, accessible from stiffness homogenization across RVE I, and of the mesopores, $\mathbb{C}_{\text{meso}\phi}$, and by the density of cracks, quantified by the so-called crack density parameter e (Budiansky and O’Connell 1976).

On *hierarchical level III*, a macroporous conglomerate material consisting of mesoporous, cracked hydroxyapatite granules and newly grown bone tissue emerges, see the top of Fig. 1: granules with the stiffness of RVE II described above and filling volume fraction $f_{\text{gran}}^{\text{congl}}$, are surrounded by layers of newly grown bone tissue, with volume fraction $f_{\text{bone}}^{\text{congl}}$ and stiffness derived from the ultrasonic tests of Ashman and van Buskirk (1987). These coated spherical elements are assembled, in mutual contact, to a granular conglomerate with macropores, with volume fraction $\phi_{\text{macro}}^{\text{congl}}$, in-between. At the time of granule implantation, no bone tissue has been formed yet, and this initial configuration is characterized by $f_{\text{bone}}^{\text{congl}} = 0$. For estimating the macroscopic stiffness tensor of the bone-scaffold conglomerate, $\mathbb{C}_{\text{congl}}$, the homogenization approach for an n -layered spherical inclusion proposed by Hervé and Zaoui (1993) is specialized for $n = 1$ (relating to bone tissue), adapted for the case that the stiffness of this layer is transversally isotropic, see (Bertrand and Hellmich 2009), and further combined with a self-consistent homogenization scheme, in order to account for mutually interacting coated spheres with porous space in-between—in absence of any explicit “matrix phase”. This homogenization step is thus based on

the composition and morphology of RVE III, as well as on the stiffness tensors of the granule material, \mathbb{C}_{gran} , accessible from stiffness homogenization across RVE II, of the bone tissue, \mathbb{C}_{bone} , and of the macropores, $\mathbb{C}_{\text{macro}\phi}$; the underlying mathematical framework is described at length in (Scheiner et al. 2016).

3 Downscaling of stresses from macro- to microscale

The stiffness homogenization scheme for the herein investigated biomaterial scaffold for mandibular regeneration, described in Sect. 2.3, constitutes the basis for stress downscaling. For conciseness, the derivation of this (mathematically extensive) model is not repeated here in minute detail; instead, we focus on elaborating how stress downscaling is achieved, while assuming that the homogenized stiffness tensors on all observation scales, compare Fig. 1, namely the stiffness tensor of the nanoporous hydroxyapatite matrix, $\mathbb{C}_{\text{polyHA}}$, the stiffness tensor of the pre-cracked, mesoporous granule material, \mathbb{C}_{gran} , and the stiffness tensor of the bone-scaffold conglomerate, $\mathbb{C}_{\text{congl}}$, are known from the respective homogenization steps. In particular, we first clarify the mechanical input parameters the employed downscaling approach is based on (see Sect. 3.1), and present then briefly the three downscaling steps in terms of the underlying mathematical framework:

1. From the macroporous bone-scaffold conglomerate to the pre-cracked and mesoporous granules (see Sect. 3.2);
2. From the pre-cracked and mesoporous granules to the microporous, polycrystalline hydroxyapatite matrix (see Sect. 3.3); and
3. From the microporous, polycrystalline hydroxyapatite matrix to single, arbitrarily oriented hydroxyapatite crystal needles (see Sect. 3.4).

3.1 Definition of mechanical input parameters

As for the underlying main elementary constituent, i.e. hydroxyapatite, the respective stiffness tensor, \mathbb{C}_{HA} , is defined via the bulk modulus, k_{HA} , and the shear modulus, μ_{HA} , $\mathbb{C}_{\text{HA}} = 3k_{\text{HA}}\mathbb{K} + 2\mu_{\text{HA}}\mathbb{J}$, with \mathbb{K} being the volumetric part of the fourth-order unit tensor \mathbb{I} , and \mathbb{J} the corresponding deviatoric part, $\mathbb{K} + \mathbb{J} = \mathbb{I}$.

Numerical values for k_{HA} and μ_{HA} are found based on the experiments performed by Katz and co-workers (Katz and Ukraincik 1971; Gilmore and Katz 1982), who revealed the Young's modulus and Poisson's ratio of hydroxyapatite, $E_{\text{HA}} = 114 \text{ GPa}$ and $\nu_{\text{HA}} = 0.27$, see also (Hellmich and Ulm 2002; Hellmich et al. 2004). Through standard relations of continuum mechanics, $k = E/[3(1-2\nu)]$ and $\mu = E/[2(1+\nu)]$ (Mang and Hofstetter 2000), one finally obtains $k_{\text{HA}} = 82.61 \text{ GPa}$ and $\mu_{\text{HA}} = 44.88 \text{ GPa}$. Furthermore, all pore spaces are assumed to be drained at all times, thus $\mathbb{C}_{\text{micro}\phi} = \mathbb{C}_{\text{meso}\phi} = \mathbb{C}_{\text{macro}\phi} = 0$.

For defining the stiffness tensor of newly formed bone tissue, \mathbb{C}_{bone} , we consider the orthotropic stiffness tensor determined for mandibular bone by means of ultrasound measurements by Ashman and van Buskirk (1987), and follow then the strategy described in (Bertrand and Hellmich 2009) for converting the ultrasound-based, anisotropic stiffness tensor into the transversally isotropic stiffness tensor related to the bone tissue growing on granules, see also (Scheiner et al. 2016) for details, yielding

$$\mathbb{C}_{\text{bone}}^{(\mathbf{e}_r, \mathbf{e}_\theta, \mathbf{e}_\varphi)} = \begin{pmatrix} 15.90 & 9.00 & 9.00 & 0 & 0 & 0 \\ 9.00 & 21.74 & 10.70 & 0 & 0 & 0 \\ 9.00 & 10.70 & 21.74 & 0 & 0 & 0 \\ 0 & 0 & 0 & 11.04 & 0 & 0 \\ 0 & 0 & 0 & 0 & 7.93 & 0 \\ 0 & 0 & 0 & 0 & 0 & 7.93 \end{pmatrix} \text{ GPa}, \quad (1)$$

with superscript $(\mathbf{e}_r, \mathbf{e}_\theta, \mathbf{e}_\varphi)$ indicating that this stiffness tensor is expressed in a spherical coordinate system, owing to the fact that in the particular case, bone tissue is added in form of a concentric shell on top of the spherical granules.

- 3.2 From the macroporous bone-scaffold conglomerate to the pre-cracked, mesoporous granules (Fig. 1, hierarchical level III)

Based on the pioneering work of Hervé and Zaoui (1993), the aforementioned stiffness homogenization scheme for granular hydroxyapatite-based biomaterials, see Sect. 2.3, gives, on the one hand, access to the volumetric stress tensor of the granule material, $\mathbb{e}_{\text{gran}}^{\text{congl, vol}}$, in response to a macroscopically applied volumetric strain tensor $\mathbb{E}_{\text{congl}}^{\text{vol}}$,

$$\sigma_{gran}^{congl,vol} = \frac{3k_{gran}\overline{\Gamma_{gran,1}^k}}{D_k} \mathbf{E}_{congl}^{vol}, \tag{2}$$

and, on the other hand, to the deviatoric stress tensor of the granule material, $\mathbf{e}_{gran}^{congl,dev}$, in response to a macroscopic strain tensor representing pure shear, $\mathbf{E}_{congl}^{shear}$,

$$\sigma_{gran}^{congl,dev} = 2\mu_{gran} \left(\overline{\Gamma_{gran,1}^\mu} - \frac{21\overline{\Gamma_{gran,2}^\mu}}{5(1-2\nu_{gran})} \right) \mathbf{E}_{congl}^{shear}, \tag{3}$$

where k_{gran} is the bulk modulus, μ_{gran} the shear modulus, and ν_{gran} the Poisson’s ratio of the granule material. Furthermore, Eqs. (2) and (3) are governed by a number of material properties, namely $\overline{\Gamma_{gran,1}^k}$, $\overline{\Gamma_{gran,1}^\mu}$, $\overline{\Gamma_{gran,2}^\mu}$, and D_k . These material properties are functions of the conglomerate’s composition (quantified by volume fractions f_{gran}^{congl} and f_{bone}^{congl}), as well as the stiffness tensors of the conglomerate consisting of scaffold material and bone tissue, \mathbf{C}_{congl} , of the granule material, \mathbf{C}_{gran} , of the added bone matrix, \mathbf{C}_{bone} , and of the macropores, $\mathbf{C}_{macro\phi}$. The somewhat unusual form of the downscaling relations given by Eqs. (2) and (3) as well as of the lengthy mathematical expressions for $\overline{\Gamma_{gran,1}^k}$, $\overline{\Gamma_{gran,1}^\mu}$, $\overline{\Gamma_{gran,2}^\mu}$, and D_k , given in detail in (Scheiner et al. 2016), result from the nature of the employed coated inclusion-problem of Hervé and Zaoui (1993), where, in contrast to the classical Eshelby-problem, the stresses and strains are *not* homogeneous throughout the inclusion.

Considering now that any strain (and, of course, also stress) tensor can be decomposed into volumetric and pure shear strain tensors, Eqs. (2) and (3) can be utilized for downscaling a general macroscopic strain tensor, \mathbf{E}_{congl} to the corresponding stress tensor experienced by the granule material,

$$\begin{aligned} \sigma_{gran}^{congl} &= \frac{3k_{gran}\overline{\Gamma_{gran,1}^k}}{D_k} \frac{\text{tr} \mathbf{E}_{congl}}{3} \mathbf{I} + 2\mu_{gran} \\ &\times \left(\overline{\Gamma_{gran,1}^\mu} - \frac{21\overline{\Gamma_{gran,2}^\mu}}{5(1-2\nu_{gran})} \right) \\ &\times \left(\mathbf{E}_{congl} - \frac{\text{tr} \mathbf{E}_{congl}}{3} \mathbf{I} \right), \end{aligned} \tag{4}$$

where tr is the trace operator, $\text{tr} \mathbf{E}_{congl} = E_{congl,11} + E_{congl,22} + E_{congl,33}$, and \mathbf{I} is the second-order unit tensor. Given that the underlying constitutive law on the observation scale of the bone-scaffold conglomerate is linear elastic, $\Sigma_{congl} = \mathbf{C}_{congl} : \mathbf{E}_{congl}$, Eq. (4)

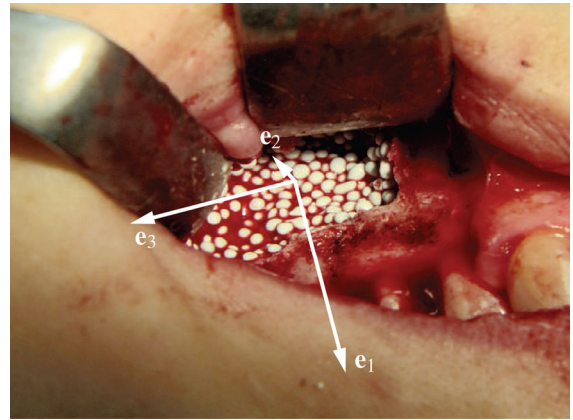


Fig. 2 Image of the studied bone-scaffold conglomerate inserted into the upper jaw, based on which the macroscopic mechanical boundary conditions of the conglomerate consisting of bone tissue-coated granules are defined: load application occurs in direction \mathbf{e}_1 (resembling mastication), deformation in direction \mathbf{e}_3 is presumably prevented, the material is stress-free in direction \mathbf{e}_2 , the conglomerate material is furthermore free of shear stresses and strains

can be straightforwardly applied for also downscaling macroscopic stress tensors to the granule material level, through substituting \mathbf{E}_{congl} by $(\mathbf{C}_{congl})^{-1} : \Sigma_{congl}$.

In the following, we want to exemplify stress downscaling, quantitatively, through prescribing macroscopically the predominant loading type expected for the studied biomaterial in physiological conditions. Typically, the biomaterial investigated in this paper is inserted from the buccal (exterior) mandible surface, and the granules-filled bone defect is covered afterwards by means of a bioresorbable membrane, see Fig. 2 (where the membrane has not yet been put in place). Considering that the macroscopic loading is usually prescribed in terms of stress component $\Sigma_{congl,11} < 0$ (relating to mastication), and that the further mechanical boundary conditions for the bone-scaffold conglomerate are $E_{congl,11} < 0$, $E_{congl,22} > 0$, $E_{congl,33} = E_{congl,12} = E_{congl,13} = E_{congl,23} = 0$, $\Sigma_{congl,33} < 0$, and $\Sigma_{congl,22} = \Sigma_{congl,12} = \Sigma_{congl,13} = 0$ gives access, via the linear elastic constitutive law, to the corresponding macroscopic stress tensor:

$$\Sigma_{congl} = \begin{pmatrix} \Sigma_{congl,11} & & & & \\ 0 & & & & \\ \frac{3k_{congl} - 2\mu_{congl}}{2(3k_{congl} + \mu_{congl})} \Sigma_{congl,11} & & & & \\ 0 & & & & \\ 0 & & & & \\ 0 & & & & \end{pmatrix}. \tag{5}$$

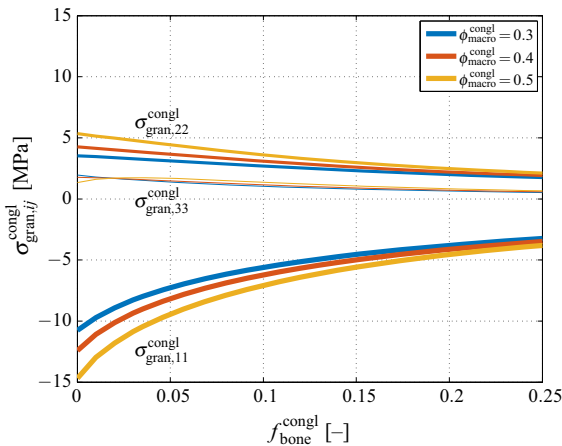


Fig. 3 Non-zero components of the stress tensor of the granule material according to Eq. (4), for varying bone tissue volume fraction f_{bone}^{congl} , and under physiologically relevant macroscopic stress according to Eq. (5), with $\Sigma_{congl,11} = -10$ MPa

In the following, the macroscopic stress tensor component in direction of base vector e_1 is set to $\Sigma_{congl,11} = -10$ MPa, while Eq. (5) gives access to the second non-zero component of the macroscopic stress tensor. Furthermore, the crack density parameter for quantifying the occurrence of cracks on hierarchical level II is set to $e = 10$ (representing a low to moderate crack density), see Sect. 3.3 for further details. The downscaling relation given by Eq. (4) provides then the corresponding stress tensor experienced by the granule material, see Fig. 3, where also the effect of increasing bone volume fraction is illustrated. Notably, the macroscopically applied biaxial loading relates to a triaxial loading on one observation scale below.

3.3 From the pre-cracked, mesoporous granules to the microporous hydroxyapatite polycrystal (Fig. 1, hierarchical level II)

For this downscaling step we can make use of classical strain and stress downscaling as defined in the framework of continuum micromechanics. As derived elsewhere, see e.g. (Zaoui 2002; Dormieux et al. 2006), continuum micromechanics allows to downscale strain tensors through the so-called concentration (or localization) tensors: for the present case, this implies that the strain tensor of the microporous hydroxyapatite polycrystal, ϵ_{polyHA}^{gran} , is related to the strain tensor of the granule material, ϵ_{gran}^{congl} , through

$$\epsilon_{polyHA}^{gran} = A_{polyHA}^{gran} : \epsilon_{gran}^{congl}, \tag{6}$$

where A_{polyHA}^{gran} is the strain concentration tensor of the microporous hydroxyapatite polycrystal. The latter is estimated by means of Eshelby’s matrix-inclusion problem (Eshelby 1957); considering the matrix-inclusion-type morphology discernible on hierarchical level II, compare Fig. 1, A_{polyHA}^{gran} is defined by (Deudé et al. 2002; Dormieux et al. 2004)

$$A_{polyHA}^{gran} = \left\{ f_{polyHA}^{gran} \mathbb{I} + \phi_{meso}^{gran} \times \left[\mathbb{I} - P_{sph}^{polyHA} : (C_{meso\phi} - C_{polyHA}) \right]^{-1} + eQ \right\}^{-1}, \tag{7}$$

where P_{sph}^{polyHA} is the fourth-order Hill tensor related to spherical inclusions embedded in a matrix exhibiting a stiffness tensor C_{polyHA} , see (Eshelby 1957; Zaoui 2002) for how P_{sph}^{polyHA} is computed. Hence, in contrast to the situation in Sect. 3.2, we here employ the Eshelby’s classical matrix-inclusion problem (Eshelby 1957). Finally, e is the so-called crack density parameter (Budiansky and O’Connell 1976), $e = \mathcal{N}(r_{crack})^3$, with \mathcal{N} as the number of cracks per volume, and r_{crack} as the (average) crack radius, and Q is a tensor defined via the Poisson’s ratio of the microporous hydroxyapatite polycrystal, ν_{polyHA} , through (Dormieux et al. 2004)

$$Q = \frac{16}{9} \frac{1 - (\nu_{polyHA})^2}{1 - 2\nu_{polyHA}} \mathbb{K} + \frac{32}{45} \frac{(1 - \nu_{polyHA})(5 - \nu_{polyHA})}{2 - \nu_{polyHA}} \mathbb{J}, \tag{8}$$

where \mathbb{J} is the devatoric part of the fourth-order unit tensor \mathbb{I} , $\mathbb{J} = \mathbb{I} - \mathbb{K}$.

Linear elasticity on all hierarchical levels implies $\epsilon_{gran}^{congl} = (C_{gran})^{-1} : \sigma_{gran}^{congl}$, as well as $\epsilon_{polyHA}^{gran} = (C_{polyHA})^{-1} : \sigma_{polyHA}^{gran}$, so that the strain concentration relation of Eq. (6) can be transformed into a fully equivalent stress concentration relation of the format

$$\sigma_{polyHA}^{gran} = B_{polyHA}^{gran} : \sigma_{gran}^{congl}, \tag{9}$$

with the stress concentration tensor of the microporous hydroxyapatite matrix, B_{polyHA}^{gran} , following from the strain concentration tensor A_{polyHA}^{gran} , through

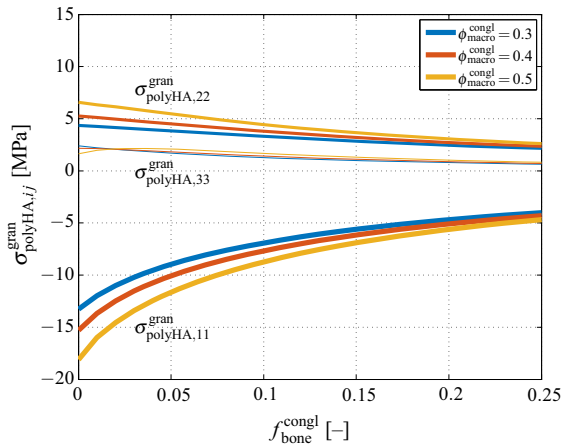


Fig. 4 Non-zero components of the stress tensor of the microporous hydroxyapatite polycrystal according to Eqs. (4) and (9), for varying bone tissue volume fraction f_{bone}^{congl} , and under physiologically relevant macroscopic stress according to Eq. (5), with $\Sigma_{congl,11} = -10$ MPa

$$\mathbb{B}_{polyHA}^{gran} = \mathbb{C}_{polyHA} : \mathbb{A}_{polyHA}^{gran} : (\mathbb{C}_{gran})^{-1}. \quad (10)$$

Downscaling of stresses according to Eq. (9) leads to further magnification of stresses; see Fig. 4 for the non-zero stress tensor components of the microporous granule material, obtained through application of Eq. (9) to the stresses depicted in Fig. 3.

3.4 From the microporous hydroxyapatite polycrystal to the single hydroxyapatite crystal (Fig. 1, hierarchical level III)

The hydroxyapatite crystals making up the the microporous hydroxyapatite polycrystal are oriented arbitrarily, in all space directions, defined by in a spherical coordinate system by Euler angles ϑ and φ , see Fig. 5. Each orientation implies different stress levels occurring in the respective hydroxyapatite crystal, $\sigma_{HA}^{polyHA} = \sigma_{HA}^{polyHA}(\vartheta, \varphi)$, for a given macroscopic loading. Making use of the orientation-dependent stress concentration tensor related to hydroxyapatite needles, $\mathbb{B}_{HA}^{polyHA}(\vartheta, \varphi)$, stress tensor $\sigma_{HA}^{polyHA}(\vartheta, \varphi)$ follows as

$$\sigma_{HA}^{polyHA}(\vartheta, \varphi) = \mathbb{B}_{HA}^{polyHA}(\vartheta, \varphi) : \sigma_{polyHA}^{gran}, \quad (11)$$

with σ_{polyHA}^{gran} following from Eq. (9).

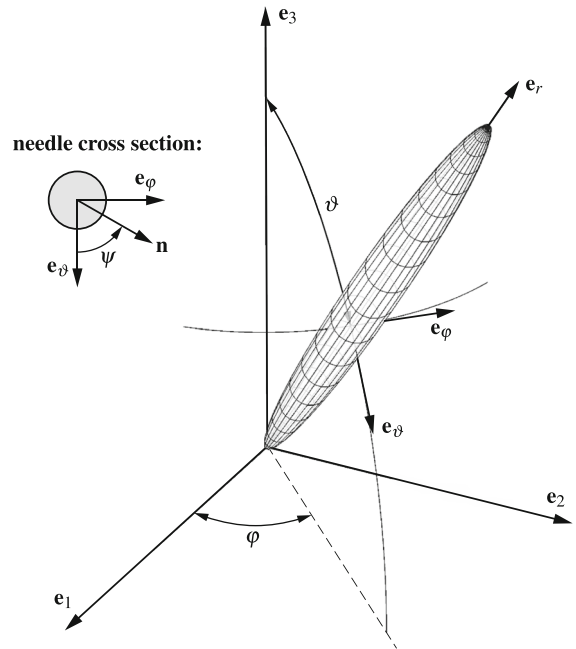


Fig. 5 Cylindrical hydroxyapatite needle oriented along vector e_r , and inclined by the Euler angles ϑ and φ , with respect to the reference base frame defined through the unit vectors e_1 , e_2 , and e_3 ; the local base frame, defined by unit vectors e_r , e_ϑ , and e_φ , is attached to the cylindrical inclusion; vector n , oriented perpendicular to e_r , is further defined by angle ψ

Stress concentration tensor $\mathbb{B}_{HA}^{polyHA}(\vartheta, \varphi)$ is defined analogously to Eq. (10),

$$\mathbb{B}_{HA}^{polyHA}(\vartheta, \varphi) = \mathbb{C}_{HA} : \mathbb{A}_{HA}^{polyHA}(\vartheta, \varphi) : (\mathbb{C}_{polyHA})^{-1}. \quad (12)$$

The orientation-dependent strain concentration tensor $\mathbb{A}_{HA}^{polyHA}(\vartheta, \varphi)$ is defined, according to (Fritsch et al. 2006), by

$$\begin{aligned} \mathbb{A}_{HA}^{polyHA}(\vartheta, \varphi) = & \left[\mathbb{I} + \mathbb{P}_{cyl}^{polyHA}(\vartheta, \varphi) : (\mathbb{C}_{HA} - \mathbb{C}_{polyHA}) \right]^{-1} \\ & : \left\{ f_{HA}^{polyHA} \left[\int_{\varphi=0}^{2\pi} \int_{\vartheta=0}^{\pi} \left[\mathbb{I} + \mathbb{P}_{cyl}^{polyHA}(\vartheta, \varphi) \right. \right. \right. \\ & : (\mathbb{C}_{HA} - \mathbb{C}_{polyHA}) \left. \left. \left. \right]^{-1} \frac{\sin \vartheta d\vartheta d\varphi}{4\pi} \right] \right. \\ & \left. + \phi_{micro}^{polyHA} \left[\mathbb{I} + \mathbb{P}_{sph}^{polyHA} : (\mathbb{C}_{micro\phi} - \mathbb{C}_{polyHA}) \right] \right\}^{-1}, \quad (13) \end{aligned}$$

with $\mathbb{P}_{cyl}^{polyHA}(\vartheta, \varphi)$ as the orientation-dependent Hill tensor relating to cylindrical inclusions embedded in

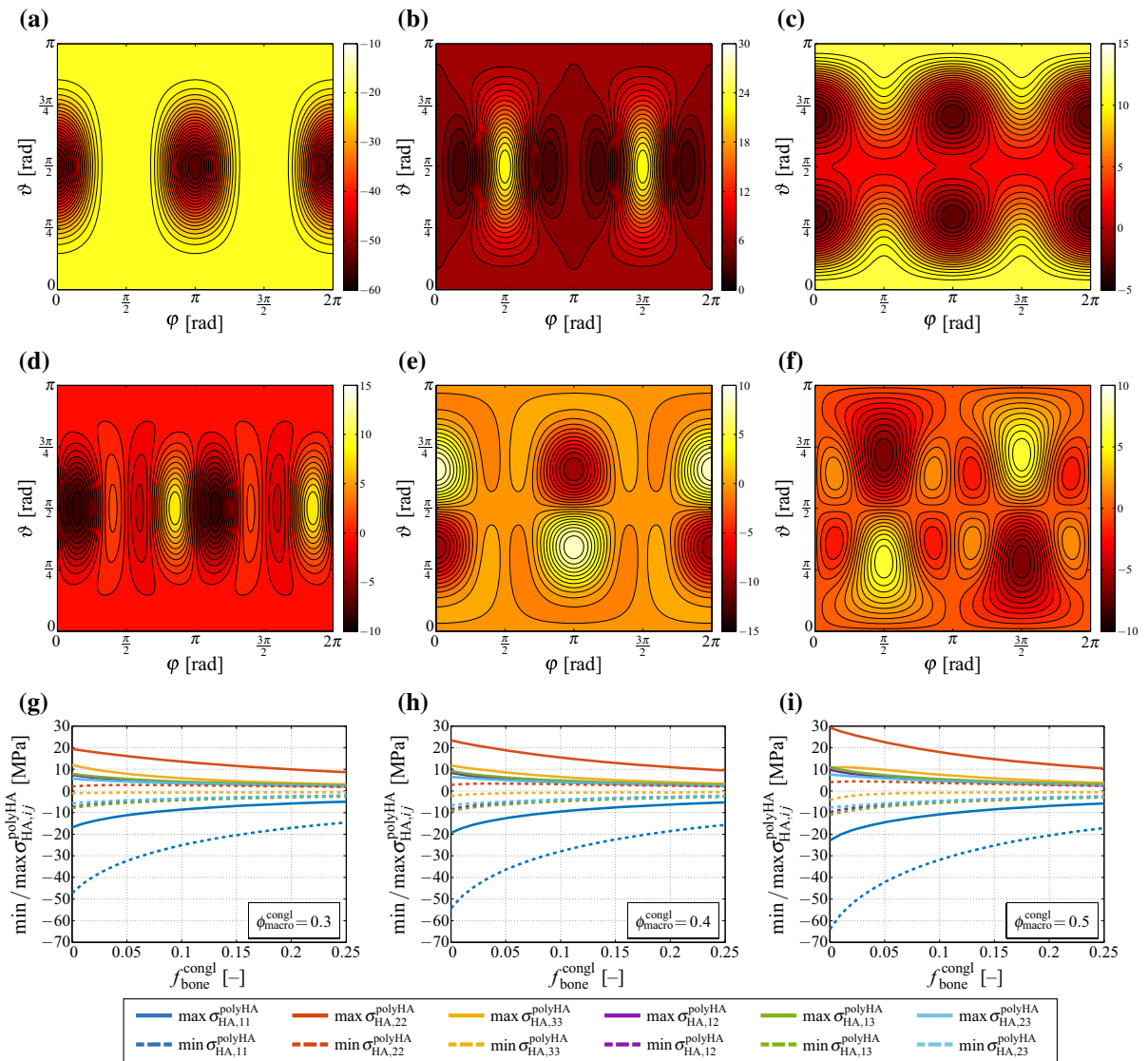


Fig. 6 Components of the stress tensor of the hydroxyapatite needles: components **a** $\sigma_{HA,11}^{polyHA}$, **b** $\sigma_{HA,22}^{polyHA}$, **c** $\sigma_{HA,33}^{polyHA}$, **d** $\sigma_{HA,12}^{polyHA}$, **e** $\sigma_{HA,13}^{polyHA}$, and **f** $\sigma_{HA,23}^{polyHA}$ as functions of the needle orientation (defined by angles ϑ and φ), for constant volume fractions of the macropores $\phi_{macro}^{congl} = 0.4$ and of bone tissue $f_{bone}^{congl} = 0$,

when feeding the macroscopic stress tensor defined by Eq. (5) into the downscaling relations given by Eqs. (4), (9), and (11) with $\Sigma_{congl,11} = -10$ MPa; **g–i** minimum and maximum values of the stress tensor components for varying macroporosities and bone tissue volume fractions

the isotropic microporous hydroxyapatite polycrystal matrix with stiffness C_{polyHA} , see (Eshelby 1957). The double integral in Eq. (13), expressing summation over all possible orientations, can be straightforwardly evaluated based on Stroud’s integration equations (Stroud 1971; Pichler et al. 2009). Notably, $A_{HA}^{polyHA}(\vartheta, \varphi)$ has been derived based on Eshelby’s famous matrix-inclusion problem (Eshelby 1957).

Feeding the composition-dependent stresses depicted in Fig. 4 into Eq. (11) reveals substantial (hydroxyapatite needle orientation-dependent) stress magnification effects, see Fig. 6. In particular, Fig. 6a–f show the variations between the different components of the hydroxyapatite stress tensor, for $\phi_{macro}^{congl} = 0.4$ and $f_{bone}^{congl} = 0$. In order to also highlight the extreme values of the stress tensor components as functions

Table 1 Minimum and maximum values of stress tensor components $\sigma_{HA,ij}^{polyHA}$, occurring when prescribing the macroscopic stress tensor given by Eq. (5), with $\Sigma_{congl,11} = -10$ MPa, compare Fig. 6g–i

ϕ_{macro}^{congl}	min $\sigma_{HA,ij}^{polyHA}$ (MPa)	max $\sigma_{HA,ij}^{polyHA}$ (MPa)
0.3	-47.24	19.41
0.4	-54.31	23.45
0.5	-63.99	29.38

of the scaffold composition, Fig. 6g–i show the minimum and maximum values of all stress tensor components over all hydroxyapatite needle orientations, see also Table 1 for an overview of the observed maximum and minimum stress tensor components. Notably, minimum stresses stresses (i.e. compressive stresses with maximum magnitude) always occur in direction \mathbf{e}_1 , while maximum stresses (i.e. tensile stresses with maximum magnitude) always occur in direction \mathbf{e}_2 .

4 Estimates for the macroscopic strength of hydroxyapatite-based granular biomaterials

4.1 Failure criterion suitable for hydroxyapatite needles

Based on the three-step scheme presented in Sect. 3, a macroscopically applied mechanical loading, prescribed in terms of macroscopic strains \mathbf{E}_{congl} or macroscopic stresses Σ_{congl} , were downscaled to the corresponding stress state experienced by a single, arbitrarily oriented hydroxyapatite needle, $\sigma_{HA}^{polyHA}(\vartheta, \varphi)$.

From (Fritsch et al. 2009a, b), we adopt that hydroxyapatite needle failure is governed by the normal stress in needle direction,

$$\sigma_{HA,rr}(\vartheta, \varphi) = \mathbf{e}_r(\vartheta, \varphi) \cdot \sigma_{HA}^{polyHA}(\vartheta, \varphi) \cdot \mathbf{e}_r(\vartheta, \varphi), \tag{14}$$

and by the shear stress in planes orthogonal to the needle direction,

$$\sigma_{HA,rn}(\vartheta, \varphi, \psi) = \mathbf{e}_r(\vartheta, \varphi) \cdot \sigma_{HA}^{polyHA}(\vartheta, \varphi) \cdot \mathbf{n}(\vartheta, \varphi, \psi). \tag{15}$$

In Eqs. (14) and (15), $\mathbf{e}_r(\vartheta, \varphi)$ denotes the vector defining the direction of a particular needle, i.e. the base

vector of the employed spherical coordinate system in radial direction, while vector $\mathbf{n}(\vartheta, \varphi, \psi)$ denotes the direction orthogonal to $\mathbf{e}_r(\vartheta, \varphi)$, additionally governed by angle ψ , compare Fig. 5. As for definition of vector $\mathbf{n}(\vartheta, \varphi, \psi)$, we consider that the needle orientation-dependent base vectors ($\mathbf{e}_r, \mathbf{e}_\vartheta, \mathbf{e}_\varphi$) are defined in the Cartesian base system ($\mathbf{e}_1, \mathbf{e}_2, \mathbf{e}_3$) as

$$\begin{aligned} \mathbf{e}_r &= (\sin \vartheta \cos \varphi, \sin \vartheta \sin \varphi, \cos \vartheta)^T, \\ \mathbf{e}_\vartheta &= (\cos \vartheta \cos \varphi, \cos \vartheta \sin \varphi, -\sin \vartheta)^T, \\ \mathbf{e}_\varphi &= (-\sin \varphi, \cos \varphi, 0)^T, \end{aligned} \tag{16}$$

and that the transformation tensor \mathbf{Q} from base system ($\mathbf{e}_1, \mathbf{e}_2, \mathbf{e}_3$) to base system ($\mathbf{e}_r, \mathbf{e}_\vartheta, \mathbf{e}_\varphi$) reads as

$$\begin{aligned} \mathbf{Q} &= (\mathbf{e}_r; \mathbf{e}_\vartheta; \mathbf{e}_\varphi)^T \\ &= \begin{pmatrix} \sin \vartheta \cos \varphi & \sin \vartheta \sin \varphi & \cos \vartheta \\ \cos \vartheta \cos \varphi & \cos \vartheta \sin \varphi & -\sin \vartheta \\ -\sin \varphi & \cos \varphi & 0 \end{pmatrix}. \end{aligned} \tag{17}$$

Then, vector $\mathbf{n}(\vartheta, \varphi, \psi)$, dependent on angles ϑ, φ , and ψ , and expressed in a Cartesian base frame, follows as

$$\mathbf{n}(\vartheta, \varphi, \psi) = \mathbf{Q}^T \cdot \begin{pmatrix} 0 \\ \cos \psi \\ \sin \psi \end{pmatrix}. \tag{18}$$

As furthermore proposed in (Fritsch et al. 2009a, b), the failure criterion for a single hydroxyapatite needles takes into account both tensile strength $\sigma_{HA}^{ult,t}$ and shear strength $\sigma_{HA}^{ult,s}$. The two strength values are accessible through analyzing the experiments of Akao et al. (1981) and Shareef et al. (1993), revealing $\sigma_{HA}^{ult,t} = 52.2$ MPa and $\sigma_{HA}^{ult,s} = 80.3$ MPa, see (Fritsch et al. 2009a). Mathematically, the failure surface related to the hydroxyapatite needles reads as

$$\begin{aligned} f_{HA}(\sigma_{HA}^{polyHA}) &= \max_{\vartheta, \varphi} \left(\frac{\sigma_{HA}^{ult,t}}{\sigma_{HA}^{ult,s}} \max_{\psi} \left| \sigma_{HA,rn}^{polyHA}(\vartheta, \varphi, \psi) \right| \right. \\ &\quad \left. + \sigma_{HA,rr}^{polyHA}(\vartheta, \varphi) \right) - \sigma_{HA}^{ult,t} = 0. \end{aligned} \tag{19}$$

Eq. (19) takes into account that for each needle orientation the angle ψ inducing the maximum tangential stress must be found, as well as the needle orientation inducing the maximum value for the combination of normal and tangential stresses. For this purpose, angles ϑ, φ , and ψ are varied between $\vartheta = 0 \dots \pi$, $\varphi = 0 \dots 2\pi$, and $\psi = 0 \dots 2\pi$. Substituting into Eq. (19) the relation between σ_{HA}^{polyHA} and Σ_{congl} , according to the downscaling scheme elaborated in Sect. 3 allows

Table 2 Iteration scheme for deriving the macroscopic loading of the biomaterial inducing quasi-brittle failure in the most unfavorably stressed hydroxyapatite needle

Iteration steps	
1.	Choice of initial value for $\Sigma_{\text{congl},11}$.
2.	Computation of macroscopic stress tensor according to Eq. (5).
3.	Downscaling of macroscopic stress tensor to the level of hydroxyapatite needles as function of the needle orientation, $\sigma_{\text{HA}}^{\text{polyHA}}(\vartheta, \varphi)$, $\vartheta = 0 \dots \pi$, $\varphi = 0 \dots 2\pi$, by means of Eqs. (2–13).
4.	Calculation of the corresponding normal and shear stress component experienced by single hydroxyapatite needles, for any needle orientation, $\vartheta = 0 \dots \pi$, $\varphi = 0 \dots 2\pi$, and for any tangential plane, $\psi = 0 \dots 2\pi$, by means of Eqs. (14–18).
5.	Evaluation of the failure criterion given by Eqs. (19) and (20), respectively: –If $f_{\text{HA}}(\Sigma_{\text{congl}}) < 0$, then $ \Sigma_{\text{congl},11} $ is increased; return to step 2. –If $f_{\text{HA}}(\Sigma_{\text{congl}}) = 0$, then the load iteration is completed, and the current magnitude for $\Sigma_{\text{congl},11}$ induces failure of the material. –If $f_{\text{HA}}(\Sigma_{\text{congl}}) > 0$, then $ \Sigma_{\text{congl},11} $ is decreased; return to step 2.

to alternatively express the failure criterion in terms of macroscopic stresses,

$$f_{\text{HA}}(\Sigma_{\text{congl}}) = 0. \tag{20}$$

4.2 Computation of composition-dependent macroscopic loading inducing hydroxyapatite needle-failure

The failure criterion presented in Sect. 4.1, for estimating the macroscopic loading that leads to quasi-brittle failure of the most unfavorably stressed hydroxyapatite needle, is evaluated in an iterative manner, see Table 2. Let us e.g. consider, for the sake of demonstration, a biomaterial configuration defined by $\phi_{\text{macro}}^{\text{congl}} = 0.4$ and $f_{\text{bone}}^{\text{congl}} = 0$. Then, the iterative approach sketched in Table 2 reveals that a macroscopic stress tensor with non-zero components $\Sigma_{\text{congl},11} = -20.31$ MPa and $\Sigma_{\text{congl},33} = -3.09$ MPa is related to $f_{\text{HA}}(\Sigma_{\text{congl}}) = 0$, thus inducing failure of the most unfavorably stressed hydroxyapatite needle. The stress state of the latter is illustrated in Fig. 7a and b, in terms of the normal and maximum shear stress components, as functions of the needle orientation. The corresponding values of the failure function $f_{\text{HA}}(\Sigma_{\text{congl}})$, as obtained through insertion of the orientation-dependent normal and maximum shear stress components into the failure criterion, is again a function of the needle orientation, as depicted in Fig. 7(c). In this figure, the needle orientations that are actually evoking the most unfavorable stress states for the aforementioned macroscopic load-

ing inducing $f_{\text{HA}}(\Sigma_{\text{congl}}) = 0$, are indicated, namely ($\varphi = 1.466$, $\vartheta = 1.676$) and ($\varphi = 4.608$, $\vartheta = 1.466$), respectively; or ($\varphi = 84.00^\circ$, $\vartheta = 96.03^\circ$) and ($\varphi = 264.03^\circ$, $\vartheta = 84.00^\circ$), respectively.

Furthermore, the magnitude of the macroscopic, material failure-inducing loading increases with increasing bone volume fraction ($f_{\text{bone}}^{\text{congl}}$), as well as with decreasing volume fraction of the macropores ($\phi_{\text{macro}}^{\text{congl}}$), see Fig. 7d.

5 Development of failure-inducing macroscopic stresses during bone regeneration

Once immersed into its targeted physiological environment, i.e. the immediate vicinity of (mandibular) bone tissue, the studied biomaterial undergoes compositional changes, due to two distinct mechanisms. On the one hand, the granules become coated with a layer of newly forming bone tissue whose thickness is growing with time. Presuming that the growth of bone tissue occurs linearly over time (Cancedda et al. 2007), the following bone volume fraction evolution law can be deduced:

$$f_{\text{bone}}^{\text{congl}} = \left[\frac{(r_{\text{gran}} + k_{\text{growth}}t)^3}{r_{\text{gran}}^3} - 1 \right] f_{\text{gran}}^{\text{congl}}, \tag{21}$$

where t is the time after placing the scaffold in a bony environment, k_{growth} is the bone growth rate, and r_{gran} is the radius of the granules. For the presently studied material, the typical bone growth rate is $k_{\text{growth}} =$

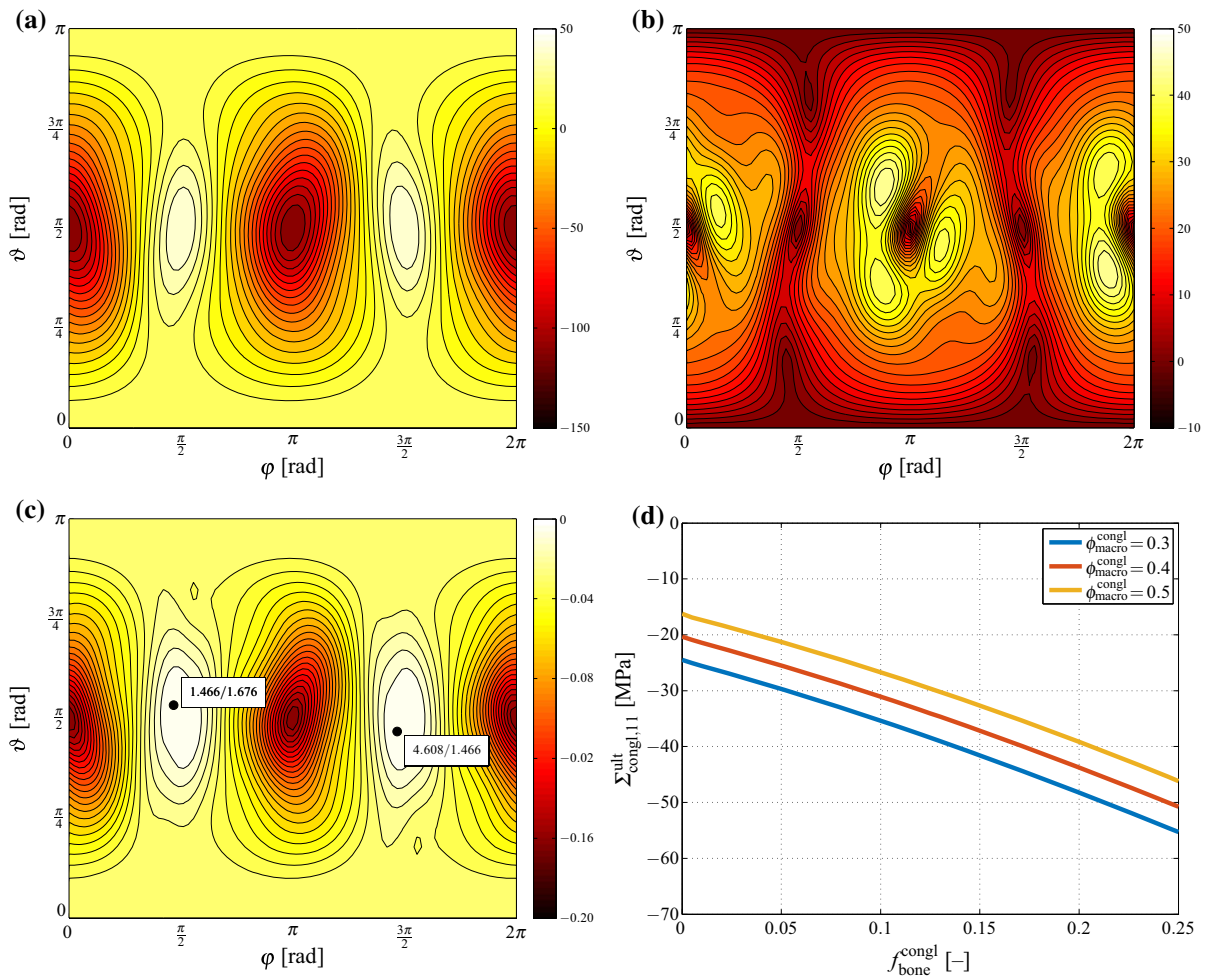


Fig. 7 **a** Normal stress component $\sigma_{HA,rr}^{polyHA}(\vartheta, \varphi)$, **b** maximum shear stress component $\max |\sigma_{HA,rsn}^{polyHA}(\vartheta, \varphi, \psi)|$, and **c** corresponding values of the failure function $f_{HA}(\Sigma_{congl})$, evaluated for $\phi_{macro}^{congl} = 0.4$, $f_{bone}^{congl} = 0$, and $\Sigma_{congl,11} = -15.15$ MPa, as

functions of the needle orientation; in **c**, the needle orientations at which $f_{HA}(\Sigma_{congl}) = 0$, are indicated; **d** the macroscopic, material failure-inducing stress tensor component $\Sigma_{congl,11}$, as function of ϕ_{macro}^{congl} and of f_{bone}^{congl}

$4 \pm 3 \mu\text{m}/\text{week}$ (Scheiner et al. 2016). The time-dependent bone tissue volume fraction defined by Eq. (21) enters, as given in great detail in (Scheiner et al. 2016), the material functions $\overline{\Gamma}_{gran,1}^k$, $\overline{\Gamma}_{gran,1}^\mu$, $\overline{\Gamma}_{gran,2}^\mu$, and \mathcal{D}_k appearing in Eqs. (2–4). In this way, Eq. (21) induces time-dependency in the strength of the investigated conglomerate material. In the same way, Eq. (21) induces time-dependencies in the homogenized stiffness expressions relating to the RVEs depicted in Fig. 1, as given in (Scheiner et al. 2016).

On the other hand, the contact of the bone-coated granules with physiological solution also leads to

resorption of hydroxyapatite. As is known from analysis of X-ray microtomography scans, this resorption process occurs via growth of the micropores (Czenek et al. 2014),

$$\phi_{micro}^{polyHA} = \phi_{micro,0}^{polyHA} + k_{res}t, \tag{22}$$

with $\phi_{micro,0}^{polyHA}$ as the microporosity before resorption sets in, and k_{res} as scaffold resorption rate. Notably, ϕ_{micro}^{polyHA} enters stress and strain downscaling at Eq. (13) of this paper, thus influencing strain concentration tensor $\mathbb{A}_{HA}^{polyHA}(\vartheta, \varphi)$, and therefore again the time-dependent strength and stiffness properties of the con-

Table 3 Values chosen for model input parameters, in order to study corresponding variations in the macroscopic failure load of bone tissue-coated hydroxyapatite-based scaffolds

Model input parameter	Unit	Numerical value (s)
Initial microporosity $\phi_{\text{micro},0}^{\text{polyHA}}$	(–)	0.445
Mesoporosity $\phi_{\text{meso}}^{\text{gran}}$	(–)	0.189
Macroporosity $\phi_{\text{macro}}^{\text{congl}}$	(–)	0.3, 0.4, 0.5
Crack density parameter e	(–)	0, 10, 25
Granule radius r_{gran}	(μm)	300, 500, 1000
Bone formation rate k_{form}	($\mu\text{m}/\text{week}$)	4, 7, 10
Scaffold resorption rate k_{res}	(week^{-1})	0, 0.008, 0.016

sidered hierarchical biomaterial. In vitro studies have shown that the resorption rate may be as high as $k_{\text{res}} = 0.016 \text{ week}^{-1}$, depending on the actual composition of the hosting medium (Scheiner et al. 2016).

In the following, a series of parametric studies are presented, for elucidating the effects of model parameter variations on the predicted development of the macroscopic failure-inducing stress tensor component in direction \mathbf{e}_1 , $\Sigma_{\text{congl},11}^{\text{ult}}$. For the sake of clarity, all model input parameters (and the variations considered for the numerical studies presented in this paper) are summarized in Table 3. The accordingly performed simulations highlight strong sensitivities of the macroscopic loading that causes failure of the hydroxyapatite needles, on the considered parameter variations, see Fig. 8. As regards the granule radius, it is striking that decreasing the radius initially implies accelerating the bone ingrowth-related increase of the load-carrying capacity, see Fig. 8a. However, the smaller the granule radius the sooner the complete pore space is filled with bone tissue, which is indicated by a peak of $\Sigma_{\text{congl},11}^{\text{ult}}$ (the actual magnitude of which depends on the macroporosity), followed by prolonged decrease of the load-carrying capacity, caused by scaffold resorption. Furthermore, it is interesting to note that the granule radius influences strongly the development of $\Sigma_{\text{congl},11}^{\text{ult}}$ directly after placing the granules in the targeted physiological environment (initiating scaffold resorption and bone formation), while the actual value of $\Sigma_{\text{congl},11}^{\text{ult}}$ at a later point of time is only governed by the macroporosity. A high macroporosity supports the strength development at mature bone regeneration states since it provides substantial space for newly added, load-carrying bone tissue; but it compromises strength before onset of

bone regeneration as well as at early regeneration states as then a comparably low amount of bone-scaffold conglomerate needs to carry all (or most) of the loading.

The scaffold resorption rate, in turn, governs both the load-carrying capacity of the bone-coated granules when the macroporosity is completely filled with new bone tissue, as well as the long-term development afterwards. Zero resorption implies that the value of $\Sigma_{\text{congl},11}^{\text{ult}}$ is maintained at a constant (maximum) level (related to complete filling of the pore space by bone matrix), whereas a non-zero resorption rate causes a long-term decrease of $\Sigma_{\text{congl},11}^{\text{ult}}$ after reaching the aforementioned maximum value, see Fig. 8b. It should be noted that this long-term decrease is caused by assuming that bone growth merely occurs on the outer surface of the (bone-covered) granules. However, in reality, it can be assumed that after substantial resorption of the hydroxyapatite crystals the physiological solution enters the micro- and mesopore spaces, leading eventually also to bone formation within the granule body. The omission of this potential additional bone formation effect can be deemed as limitation of our model.

Similar to the granule radius, the bone formation rate only influences the time span until the whole macropore space is filled with bone tissue; the long-term development of the load-carrying capacity is unaffected, see Fig. 8c.

Remarkable effects are revealed when varying the crack density parameter e , see Fig. 8d. In particular, decreasing the crack density parameter leads to a significantly increased stiffness of the granule material. Considering that in a composite material (such as the material studied in this paper) stiffer constituents attract larger fractions of a macroscopically applied loading than softer constituents, which attract lower fractions of the macroscopic loading, a granule material containing less cracks hence transfers higher stresses to the hydroxyapatite needles than those with more cracks. This eventually implies that increasing the crack density in the granule material leads to an increased load-carrying capacity. This possibly counterintuitive conclusion straightforwardly suggests that future extensions of the here presented model should comprise formulation of a failure criterion related to the bone tissue as well, in order to improve the significance of the model-predicted load-carrying capacity.

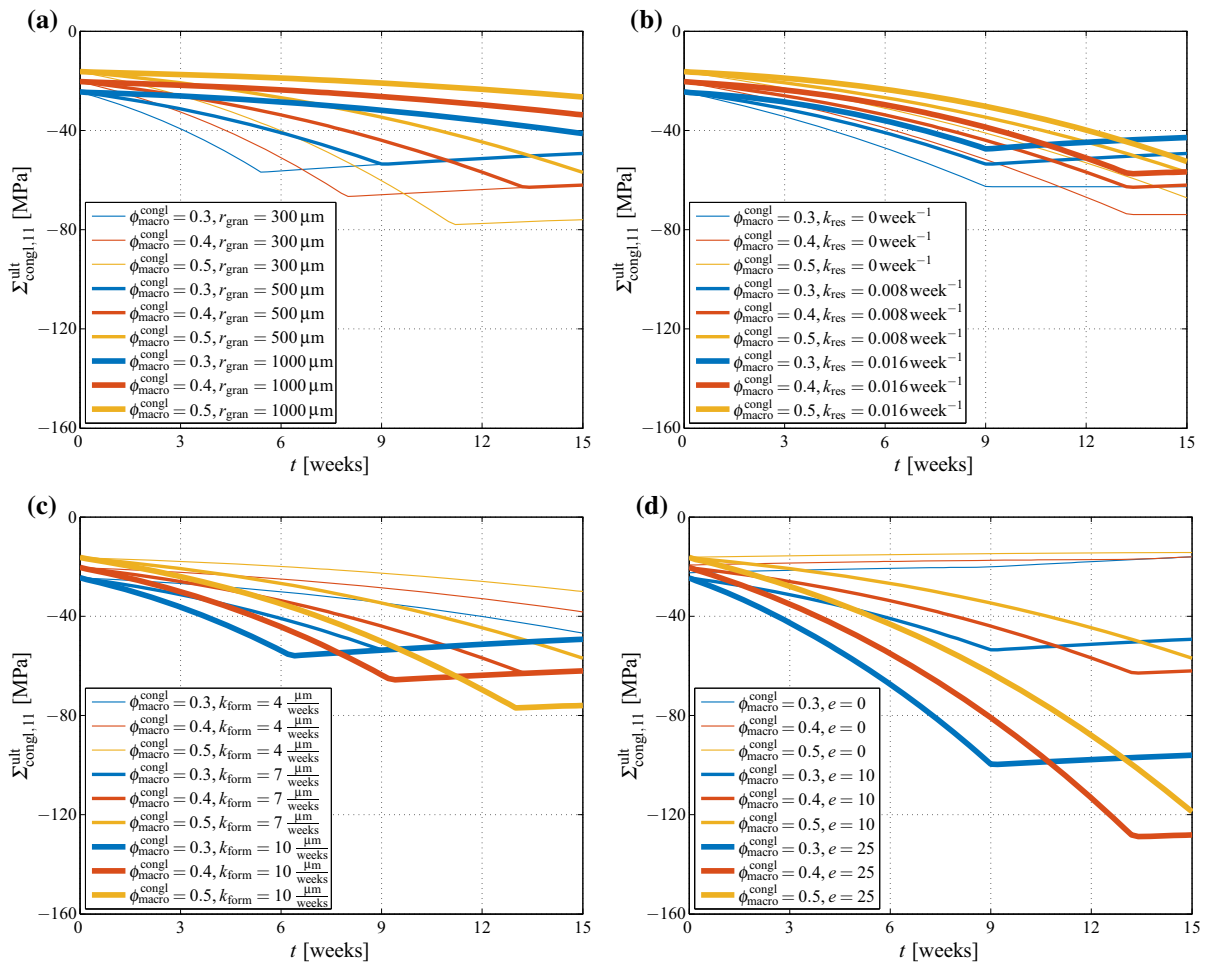


Fig. 8 Development of $\Sigma_{congl,11}^{ult}$ over time due to bone ingrowth and scaffold resorption, as function of the macroporosity ϕ_{macro}^{congl} , $\phi_{macro}^{congl} = \{0.3, 0.4, 0.5\}$, as well as of **a** the granule radius r_{gran} ,

$r_{gran} = \{300, 500, 1000 \mu m\}$, **b** the scaffold resorption rate k_{res} , $k_{res} = \{0, 0.008, 0.016 \text{ week}^{-1}\}$, **c** the bone formation rate k_{form} , $k_{form} = \{4, 7, 10 \mu m/\text{week}\}$, and **d** the crack density parameter e , $e = \{0, 10, 25\}$

6 Discussion and concluding remarks

In this paper, a continuum micromechanics-based model was presented for estimating the macroscopic loading acting onto a hydroxyapatite-based granular biomaterial, developed for application as bone replacement material (in mandibular bone), that leads to quasi-brittle failure of the material’s main constituent, i.e. hydroxyapatite crystals. The parametric studies presented in Sect. 5 show how the load-carrying capacity of the studied biomaterial develops over time once placed in the targeted physiological environment, i.e. the immediate vicinity of mandibular bone, consider-

ing the growth of new bone tissue on the surface of the scaffold material, and resorption of the hydroxyapatite needles. Thereby, main emphasis was on highlighting the influence of specific design parameters of the production process, e.g. the exact chemical composition of the biomaterial might influence the rates of bone ingrowth and scaffold resorption, the crack density may be related to the production process, and the macroporosity can be tuned based on the packing density of the granules. From a practical point of view, the presented modeling approach allows to determine from when onwards a particular area of the mandible including an implant composed of the studied biomaterial can

be used for mastication if the mechanical loading acting onto this mandibular region is approximately known, e.g. from Finite Element simulations (Korioth et al. 1992; Meijer et al. 1993; Choi et al. 2005; Hellmich et al. 2008; Bevilacqua et al. 2011).

However, the simulation results also point out two model restrictions. On the one hand, the kind of counterintuitive observation was made that a severely cracked granule material implies that the bone tissue growing on the granule surface attracts most of the macroscopically applied stress. Thus, our model suggests that increasing the crack density leads to an increasing load-carrying capacity, owing to the fact that the employed failure criterion considers only the most unfavorably stressed hydroxyapatite needle contained in the granules, neglecting however the stress experienced by the newly formed bone tissue. On the other hand, our model does not consider that the dissolution of hydroxyapatite needles would eventually lead to morphological changes in the microporous hydroxyapatite matrix (hierarchical level I in compare Fig. 1), implying that physiological solution could enter the micropore space, facilitating there bone tissue formation. Given that the described model inadequacies become relevant only after a certain (not yet quantifiable) time span, but not directly after scaffold implantation, leads to the conclusion that our model is particularly accurate for early-age bone-scaffold conglomerates (with respect to the time instant when the granules are placed into the targeted physiological environment), while the prediction accuracy presumably diminishes over time. This restriction constitutes the basis for reasonable future research directions.

Finally, it is also important to discuss the relevance of traditional fracture mechanics approaches, typically focusing on the prediction of crack propagation, thus assuming the existence of an initial crack (Müller et al. 2002; Näser et al. 2007; Kolednik et al. 2010; Ott et al. 2010), in the context of the material studied in this paper. Actually, it seems to be a worthwhile subject of future research activities to extend the micromechanics-based assessment of specific, microscopically sized material constituents (as demonstrated in this paper) towards traditional fracture mechanics, see e.g. (Pichler et al. 2007; Pichler and Dormieux 2009b, a). Such extension would be particularly relevant for mature bone-scaffold conglomerates containing already a substantial amount of bone tissue, allowing for studying the effects of crack emergence and

propagation in the bone tissue—given that a respective failure criterion has been formulated, see e.g. (Fritsch et al. 2009b)—as well as of biologically driven crack healing.

Acknowledgements Open access funding provided by Vienna University of Technology. Partial financial support by the European Research Council (ERC), in the framework of the project *Multiscale poromicromechanics of bone materials, with links to biology and medicine* (project number FP7-257023), as well as the partial financial support by the Russian Science Foundation (Grant Number 15-13-00108), are gratefully acknowledged. Furthermore, COST-action MP1005, *NAMABIO—From nano to macro biomaterials (design, processing, characterization, modeling) and applications to stem cells regenerative orthopedic and dental medicine* has provided means for a sustainable cooperation over several years.

Open Access This article is distributed under the terms of the Creative Commons Attribution 4.0 International License (<http://creativecommons.org/licenses/by/4.0/>), which permits unrestricted use, distribution, and reproduction in any medium, provided you give appropriate credit to the original author(s) and the source, provide a link to the Creative Commons license, and indicate if changes were made.

References

- Akao M, Aoki H, Kato K (1981) Mechanical properties of sintered hydroxyapatite for prosthetic applications. *J Mater Sci* 16(3):809–812
- Ashman R, van Buskirk W (1987) The elastic properties of a human mandible. *Adv Dental Res* 1(1):64–67
- Benveniste Y (1987) A new approach to the application of Mori-Tanaka's theory in composite materials. *Mech Mater* 6:147–157
- Bertrand E, Hellmich C (2009) Multiscale elasticity of tissue engineering scaffolds with tissue-engineered bone: a continuum micromechanics approach. *J Eng Mech (ASCE)* 135(5):395–412
- Bevilacqua M, Tealdo T, Menini M, Pera F, Mossolov A, Drago C, Pera P (2011) The influence of cantilever length and implant inclination on stress distribution in maxillary implant-supported fixed dentures. *J Prosthet Dent* 105(1):5–13
- Budiaknsy B, O'Connell R (1976) Elastic moduli of a cracked solid. *Int J Solids Struct* 12(2):81–97
- Burg K, Porter S, Kellam J (2000) Biomaterial developments for bone tissue engineering. *Biomaterials* 21(23):2347–2359
- Cancedda R, Cedola A, Giuliani A, Komlev V, Lagomarsino S, Mastrogiacomo M, Peyrin F, Rustichelli F (2007) Bulk and interface investigations of scaffolds and tissue-engineered bones by X-ray microtomography and X-ray microdiffraction. *Biomaterials* 28(15):2505–2524
- Choi A, Ben-Nissan B, Conway R (2005) Three-dimensional modelling and finite element analysis of the human mandible during clenching. *Aust Dental J* 50(1):42–48

- Czenek A, Blanchard R, Dejaco A, Sigurjónsson O, Örylgsson G, Gargiulo P, Hellmich C (2014) Quantitative intravoxel analysis of micro-CT-scanned resorbing ceramic biomaterials—perspectives for computer-aided biomaterial design. *J Mater Res* 29(23):2757–2772
- Dejaco A, Komlev V, Jaroszewicz J, Swieszkowski W, Hellmich C (2012) Micro CT-based multiscale elasticity of double-porous (pre-cracked) hydroxyapatite granules for regenerative medicine. *J Biomech* 45(6):1068–1075
- Dejaco A, Komlev V, Jaroszewicz J, Swieszkowski W, Hellmich C (2016) Fracture safety of double-porous hydroxyapatite biomaterials. *Bioinspired Biomim Nanobiomater*. <http://www.icevirtuallibrary.com/doi/abs/10.1680/jbibn.15.00021>
- Deudé V, Dormieux L, Kondo D, Maghous S (2002) Micromechanical approach to nonlinear poroelasticity: application to cracked rocks. *J Eng Mech (ASCE)* 128(8):848–855
- Dormieux L, Lemarchand E, Kondo D, Fairbairn E (2004) Elements of poro-micromechanics applied to concrete. *Mater Struct/Concrete Sci Eng* 37(265):31–42
- Dormieux L, Kondo D, Ulm FJ (2006) *Microporomechanics*. Wiley, Chichester
- Drugan W, Willis J (1996) A micromechanics-based nonlocal constitutive equation and estimates of representative volume element size for elastic composites. *J Mech Phys Solids* 44(4):497–524
- Eshelby J (1957) The determination of the elastic field of an ellipsoidal inclusion, and related problems. *Proc R Soc Lond Ser A* 241:376–396
- Fritsch A, Hellmich C (2007) ‘Universal’ microstructural patterns in cortical and trabecular, extracellular and extravascular bone materials: micromechanics-based prediction of anisotropic elasticity. *J Theor Biol* 244(4):597–620
- Fritsch A, Dormieux L, Hellmich C (2006) Porous polycrystals built up by uniformly and axisymmetrically oriented needles: homogenization of elastic properties. *Comptes Rendus Mécanique* 334(3):151–157
- Fritsch A, Dormieux L, Hellmich C, Sanahuja J (2009a) Mechanical behavior of hydroxyapatite biomaterials: an experimentally validated micromechanical model for elasticity and strength. *J Biomed Mater Res Part A* 88A(1):149–161
- Fritsch A, Hellmich C, Dormieux L (2009b) Ductile sliding between mineral crystals followed by rupture of collagen crosslinks: experimentally supported micromechanical explanation of bone strength. *J Theor Biol* 260(2):230–252
- Gilmore R, Katz J (1982) Elastic properties of apatites. *J Mater Sci* 17(4):1131–1141
- Hellmich C, Ulm FJ (2002) Micromechanical model for ultrastructural stiffness of mineralized tissues. *J Eng Mech (ASCE)* 128(8):898–908
- Hellmich C, Ulm FJ, Dormieux L (2004) Can the diverse elastic properties of trabecular and cortical bone be attributed to only a few tissue-independent phase properties and their interactions? Arguments from a multiscale approach. *Bio-mech Model Mechanobiol* 2(4):219–238
- Hellmich C, Kober C, Erdmann B (2008) Micromechanics-based conversion of CT data into anisotropic elasticity tensors, applied to FE simulations of a mandible. *Ann Biomed Eng* 36(1):108–122
- Hervé E, Zaoui A (1993) n-Layered inclusion-based micromechanical modelling. *Int J Eng Sci* 31(1):1–10
- Hill R (1963) Elastic properties of reinforced solids: some theoretical principles. *J Mech Phys Solids* 11(5):357–372
- Hill R (1965) A self-consistent mechanics of composite materials. *J Mech Phys Solids* 13(4):213–222
- Katz J, Ukraincik K (1971) On the anisotropic elastic properties of bone. *Calcif Tissue Int* 4(3):221–227
- Klein-Nulend J, Bacabac R, Mullender M (2005) *Mechanobiology of bone tissue*. *Pathol Biol* 53(10):576–580
- Kohlhauser C, Hellmich C (2013) Ultrasonic contact pulse transmission for elastic wave velocity and stiffness determination: influence of specimen geometry and porosity. *Eng Struct* 47:115–133
- Kolednik O, Schöngrundner R, Fischer F (2010) A new view on J-integrals in elastic-plastic materials. *Int J Fract* 187(1):77–107
- Komlev V, Barinov S, Koplík E (2002) A method to fabricate porous spherical hydroxyapatite granules intended for time-controlled drug release. *Biomaterials* 23(16):3449–3454
- Komlev V, Barinov S, Girardin E, Oscarsson S, Rosengren A, Rustichelli F, Orlovskii V (2003) Porous spherical hydroxyapatite and fluorhydroxyapatite granules: processing and characterization. *Sci Technol Adv Mater* 4(6):503–508
- Korioth T, Romilly D, Hannam A (1992) Three-dimensional finite element stress analysis of the dentate human mandible. *Am J Phys Anthropol* 88(1):69–92
- Laws N (1977) The determination of stress and strain concentrations at an ellipsoidal inclusion in an anisotropic material. *J Elast* 7(1):91–97
- Laws N (1985) A note on penny-shaped cracks in transversely isotropic materials. *Mech Mater* 4(2):209–212
- Mang H, Hofstetter G (2000) *Festigkeitslehre [Strength of materials]*. Springer, Wien
- Meijer H, Starmans F, Steen W, Bosman F (1993) A three-dimensional finite element analysis of bone around dental implants in an edentulous human mandible. *Arch Oral Biol* 38(6):491–496
- Mori T, Tanaka K (1973) Average stress in matrix and average elastic energy of materials with misfitting inclusions. *Acta Metall* 21(5):571–574
- Müller R, Kolling S, Gross D (2002) On configurational forces in the context of the finite element method. *Int J Num Methods Eng* 53(7):1557–1574
- Näser B, Kaliske M, Müller R (2007) Material forces for inelastic models at large strains: application to fracture mechanics. *Comput Mech* 40(6):1005–1013
- Ott I, Kienzler R, Schröder R (2010) Aging in the cortical bone: a constitutive law and its application. *Arch Appl Mech* 80(5):527–541
- Pichler B, Dormieux L (2009a) Instability during cohesive zone growth. *Eng Fract Mech* 76(11):1729–1749
- Pichler B, Dormieux L (2009b) Micromechanical interpretation of the dissipation associated with mode I propagation of microcracks in brittle materials. *J Appl Mech Trans ASME* 76(4):1–12
- Pichler B, Hellmich C, Mang H (2007) A combined fracture-micromechanics model for tensile strain-softening in brittle materials, based on propagation of interacting microcracks. *Int J Num Anal Methods Geomech* 31(2):111–132
- Pichler B, Hellmich C, Eberhardsteiner J (2009) Spherical and acicular representation of hydrates in a micromechanical

- model for cement paste: prediction of early-age elasticity and strength. *Acta Mech* 203(3–4):137–162
- Porter J, Ruckh T, Popat K (2009) Bone tissue engineering: a review in bone biomimetics and drug delivery strategies. *Biotechnol Prog* 25(6):1539–1560
- Reichert J, Hutmacher D (2011) Tissue engineering—from lab to clinic. In: Pallua N, Suschek C (eds) *Bone tissue engineering*, Springer, Berlin, pp 431–456
- Scheiner S, Komlev V, Gurin A, Hellmich C (2016) Multi-scale mathematical modeling in dental tissue engineering: towards computer-aided design of a regenerative system based on hydroxyapatite granules, focusing on early and mid-term stiffness recovery. *Front Physiol* 7(383):1–18
- Shareef M, Messer P, van Noort R (1993) Fabrication, characterization and fracture study of a machinable hydroxyapatite ceramic. *Biomaterials* 14(1):69–75
- Stroud A (1971) *Approximate calculation of multiple integrals*. Prentice-Hall, Englewood Cliffs
- Suquet P (1997) *Continuum micromechanics, CISM courses and lectures, vol 377*. Springer, Wien
- Velasco M, Narváez-Tovar C, Garzón-Alvarado D (2015) Design, materials, and mechanobiology of biodegradable scaffolds for bone tissue engineering. *BioMed Res Int* 729076:1–21
- Zaoui A (1997) Structural morphology and constitutive behavior of microheterogeneous materials. In: Suquet P (ed) *Continuum micromechanics*. Springer, Wien, pp 291–347
- Zaoui A (2002) Continuum micromechanics: survey. *J Eng Mech (ASCE)* 128(8):808–816